ADVANCES IN ATMOSPHERIC SCIENCES, VOL. 32, OCTOBER 2015, 1419–1430

A Diagnostic Study of the Asymmetric Distribution of Rainfall during the Landfall of Typhoon Haitang (2005)

YUE Caijun*[1], GAO Shouting[2,3], LIU Lu[2,3], and LI Xiaofan[4]

[1]*Shanghai Typhoon Institute, China Meteorological Administration, Shanghai* 200030
[2]*Institute of Atmospheric Physics, Chinese Academy of Sciences, Beijing* 100029
[3]*University of Chinese Academy of Sciences, Beijing* 100049
[4]*Department of Earth Sciences, Zhejiang University, Hangzhou* 310027

(Received 11 November 2014; revised 30 March 2015; accepted 17 April 2015)

ABSTRACT

The precipitation during landfall of typhoon Haitang (2005) showed asymmetric structures (left side/right side of the track). Analysis of Weather Research and Forecasting model simulation data showed that rainfall on the right side was more than 15 times stronger than on the left side. The causes were analyzed by focusing on comparing the water vapor flux, stability and upward motion between the two sides. The major results were as follows: (1) Relative humidity on both sides was over 80%, whereas the convergence of water vapor flux in the lower troposphere was about 10 times larger on the right side than on the left side. (2) Both sides featured conditional symmetric instability [MPV (moist potential vorticity) <0], but the right side was more unstable than the left side. (3) Strong (weak) upward motion occurred throughout the troposphere on the right (left) side. The $\boldsymbol{Q}$ vector diagnosis suggested that large-scale and mesoscale forcing accounted for the difference in vertical velocity. Orographic lift and surface friction forced the development of the asymmetric precipitation pattern. On the right side, strong upward motion from the forcing of different scale weather systems and topography caused a substantial release of unstable energy and the transportation of water vapor from the lower to the upper troposphere, which produced torrential rainfall. However, the above conditions on the left side were all much weaker, which led to weaker rainfall. This may have been the cause of the asymmetric distribution of rainfall during the landfall of typhoon Haitang.

Key words: landfall, typhoon, rainfall, asymmetric distribution, water vapor, atmospheric stability, vertical motion

Citation: Yue, C. J., S. T. Gao, L. Liu, and X. F. Li, 2015: A diagnostic study of the asymmetric distribution of rainfall during the landfall of typhoon Haitang (2005). *Adv. Atmos. Sci.*, **32**(10), 1419–1430, doi: 10.1007/s00376-015-4246-0.

1. Introduction

The heavy rainfall that occurs during the landfall of tropical cyclones (TCs) often has disastrous consequences, such as flooding and debris flow. On the other hand, they can also ease drought during hot summers. Predicting the occurrence and development of TCs is therefore important, but the asymmetric distribution of the rainfall during landfall makes this task difficult. Furthermore, such a rainfall distribution varies among different TCs.

Cline (1926) analyzed the hourly precipitation data within 500 km of hurricane centers from eight moving hurricanes and three stationary hurricanes and found that the rainfall was distributed on the front-right side for moving hurricanes and at the rear for stationary hurricanes. Miller (1958) analyzed 16 hurricanes over Florida and showed that the rain rates ahead of the center were greater than those to the rear, which was later proved by Marks (1985). Frank (1977) conducted a composite analysis of 21 years of rawinsonde data from 13 islands over the Northwest Pacific and found that rainfall was distributed more in the right-rear quadrant. Similarly, Chen and Ding (1979), Chen and Meng (2001) and Chen et al. (2002, 2004) showed that the rainfall and rainfall area of landfalling typhoons was larger on the right side than on the left side along their tracks, which was also found by Powell (1987) on the basis of hurricane Alicia (1983). In contrast, Parrish et al. (1982) found that the strongest rainfall was located on the left side of hurricane Frederic (1979) during landfall, and a similar conclusion was also reached by Wu et al. (2011) and Wang et al. (2012) based upon typhoon Morakot (2009) across Taiwan. These previous studies suggest that the asymmetric distribution characteristics of rainfall during the landfall of TCs is not always consistent among different cases. Thus, it is important to investigate the physical processes involved.

In terms of the reasons for the asymmetric distribution of rainfall, Dunn and Miller (1964) speculated that, due to the contrast in surface friction between land and sea in the Northern Hemisphere, convergence will occur on the right side of

* Corresponding author: YUE Caijun
Email: yuecaijun2000@163.com

landfalling TCs, causing the strong rainfall rate in that area. Tuleya and Kurihara (1978) supported Dunn's speculation with idealized experiments that showed that the coastward moisture advection and convergence at the boundary layer gave rise to precipitation on the right side. Tao (1980) and Si (1990) also found that, because of coastal terrain forcing, rainfall was stronger on the right side than on the left side. Similarly, Powell (1982), Jones (1987) and Chan and Liang (2003) proposed that, in addition to frictional convergence, the effects of local orography should also be considered. Niu et al. (2005) simulated typhoon Sinlaku (2002) and showed that, due to topography, rainfall was enhanced over the windward side, whereas it was weakened over the leeward side. Ji et al. (2007) also suggested the important role of topography in the production of the asymmetric distribution of rainfall generated by typhoons. Yang et al. (2011) simulated typhoon Nari (2001) and showed that the symmetric structures of the typhoon changed into asymmetric structures during and after its landfall in Taiwan because of the local topography. Thus, topography is an important factor affecting the distribution of rainfall during the landfall of TCs.

On the other hand, the influence of atmospheric factors cannot be ignored. Tao et al. (1994) linked the asymmetric distribution of rainfall to asymmetrical patterns in dynamic and thermodynamic atmospheric structures. Wang et al. (2007) studied the formation of the asymmetric rainfall of Matsa (2005) in terms of vertical velocity, vorticity, potential pseudo-equivalent temperature, water vapor flux, and dry cold airflow intrusion. Li et al. (2007) performed a diagnostic study of typhoon Imbudo (2003) and showed that the asymmetric low-level flow field led to the asymmetry in vorticity, divergence and vertical velocity in the lower troposphere, which caused the asymmetric distribution of moisture convergence and upward motion, and thus the asymmetric distribution of rainfall. The aforementioned studies have enhanced our understanding of the mechanisms involved in the formation of the asymmetric distribution of rainfall during the landfall of TCs, which in turn has contributed to improvements in precipitation forecasts.

Haitang (2005) is a typical example of a typhoon showing an asymmetric structure in its rainfall during landfall, which took place in Fujian Province, China. Yue et al. (2008) analyzed the IR1 infrared cloud imagery and found that dynamic factors were more important than thermodynamic factors. Yue (2009a) simulated Haitang (2005) and found that the asymmetric rainfall distribution was mainly associated with asymmetry in the upward motion, itself caused by asymmetry in the distribution of atmospheric forcing. Indeed, recently, Yue and Cao (2014) also concluded that atmospheric forcing plays an important role in the formation and development of asymmetric structures. Ding et al. (2009) and Wang et al. (2010) described the breakdown of rainband-enhanced asymmetric precipitation, and concluded that such a breakdown is related to both topography and the interactions between the typhoon and midlatitude systems in the upper troposphere.

The aforementioned studies discussed the cause of the asymmetric distribution of rainfall during the landfall of typhoon Haitang (2005), but none of them provided comparisons between the two sides of the storm track in terms of any physical variables/parameters. Thus, in the present reported work, we analyzed the effects of stability and different scales, through diagnosis of the moist potential vorticity (MPV) and $\boldsymbol{Q}$ vector, as well as terrain forcing, on the asymmetric rainfall distribution of typhoon Haitang (2005). In the next section, the asymmetric distribution characteristics of the rainfall and numerical simulation are described. The diagnostic methods, such as MPV, $\boldsymbol{Q}$ vector partitioning and terrain forcing are described in section 3. The results from the diagnosis of water vapor, stability and upward motion are presented in section 4 and, finally, a summary of the key findings is provided in section 5.

2. Observed rainfall structure and its simulation

2.1. *Asymmetric structure of Haitang's (2005) rainfall*

Typhoon Haitang (2005) moved across the Taiwan Strait and made landfall in Fujian Province, China, in 2005 (Fig. 1a). There was an asymmetric distribution of the associated rainfall over the land (Fig. 1b) for 24 h before and after landfall (0000 UTC 19 to 0000 UTC 20 July 2005). Figure 1b shows that the rainfall of greater than 10 mm was mainly located over the northern coastlines of Fujian Province, Zhejiang Province and southeastern Anhui Province. Meanwhile, the rainfall of greater than 50 mm occurred over the northeast coast of Fujian Province and the coast and northern region of Zhejiang Province, and the rainfall of greater than 200 mm occurred over Zhejiang Province, where the two largest rainfall amounts were 411 mm at (28.1°N, 121°E) and 336 mm at (27.9°N, 120.5°E). However, on the left side of the typhoon track, in southern Fujian Province and Guangdong Province, less than 10 mm of rainfall was recorded. Thus, there was an asymmetric structure to typhoon Haitang's rainfall during landfall.

Also of note is that the height of the topography reaches 600 m in Fujiang and Zhejiang provinces (Fig. 1a). The height was almost the same on both sides of the typhoon. The orientation of the terrain in this region is northeast–southwest, along the coast. Previous studies (Tuleya and Kurihara, 1978; Bender et al., 1985; Lin et al., 2002) have indicated that the terrain and surface friction play important roles in determining the distribution and variation of precipitation. Thus, we studied the impacts of the terrain on the asymmetric distribution of the rainfall associated with typhoon Haitang (2005).

2.2. *Numerical simulation*

The Weather Research and Forecasting (WRF) model is a new mesoscale model developed by U.S. meteorological communities. In this study, version 2.0 of the WRF model was used to simulate typhoon Haitang (2005). The initial and lateral boundary conditions were from the Global Forecast

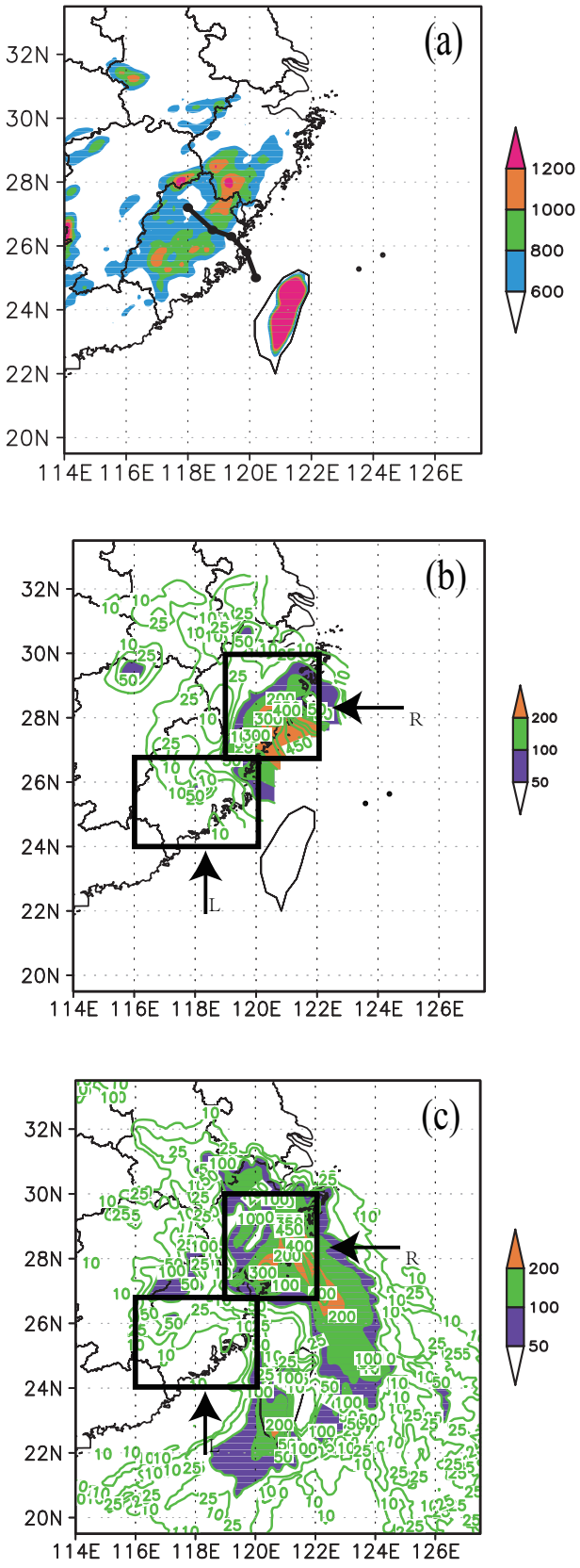

Fig. 1. Typhoon track (thick line) and terrain distribution (color scale; units: m) (a) and the 24 h accumulated (b) observed and (c) simulated rainfall (units: mm).

System reanalysis dataset (horizontal resolution: $1° \times 1°$). The simulation did not have a "bogus" scheme. Two-way nested grids were used; the fine grid mesh was 15 km and the grid number was 121×121, while the coarse grid mesh was 45 km and the grid number 81×81. The number of vertical levels was 31. The dynamical core option of the simulation was based on the advanced research WRF core (Eulerian mass-coordinate), and the main physics options consisted of the Yonsei University planetary boundary layer scheme (Hong and Pan, 1996), the Kain–Fritsch (new Eta) cumulus parameterization scheme (Kain and Frisch, 1993), the Lin et al. (1983) microphysics process scheme, the Rapid Radiative Transfer Model longwave radiation scheme (Malwer et al., 1997), the Dudhia shortwave radiation scheme (Dudhia, 1989), and a surface layer thermal diffusion scheme (Ek et al., 2003). The same physics processes were adopted for both the coarse and fine grid meshes.

The model was integrated from 0000 UTC 19 July to 0000 UTC 20 July (a total of 24 h). The simulated 24-h rainfall is shown in Fig. 1c. Compared with observation (Fig. 1b), the greater than 10 mm rainfall in the simulation was similar, and the greater than 50 mm rainfall mainly occurred in Zhejiang Province—apart from that in northwestern Zhejiang Province and southeastern Anhui Province, where the simulated rainfall was stronger than observed. The rainfall of greater than 200 mm occurred over Zhejiang Province and, specifically, rainfall peaks of 463 mm at (28.1°N, 121°E) and 343 mm at (27.9°N, 120.5°E) were simulated, which was consistent with observation.

Overall, the simulated and observed rainfall showed good agreement. Thus, we analyzed the model data to facilitate the following discussion. In the analysis that follows, the right side (26.5°–30°N, 119°–122°E) is referred to as the "R region" and the left side (24°–26.5°N, 116°–120°E) as the "L region" (Figs. 1b and c). Figure 2 shows the simulated hourly averaged rain rate in the R and L regions. The hourly rain rate in the R region ranged from 2.4 to 8.8 mm h^{-1}, and the average rain rate was 6.2 mm h^{-1}. Meanwhile, the hourly rain rate in the L region ranged from 0.2 to 0.6 mm h^{-1}, and the average rain rate was 0.4 mm h^{-1}. This clearly shows the difference in rainfall between the right and left sides of the typhoon.

3. Diagnosis methodology

3.1. *MPV theory*

The evolution of rainfall is associated with atmospheric stability, which can be measured by MPV (Bennetts and Hoskins, 1979). Under the assumption that the horizontal variation of vertical velocity is much larger than the vertical shear of horizontal velocity, and the horizontal change of vertical velocity ω is ignored, the MPV equation (Wu et al., 1995) can be expressed as

$$\mathrm{MPV} = -g(\xi_p + f)\frac{\partial \theta_e}{\partial p} + g\frac{\partial v}{\partial p}\frac{\partial \theta_e}{\partial x} - g\frac{\partial u}{\partial x}\frac{\partial \theta_e}{\partial y}, \quad (1)$$

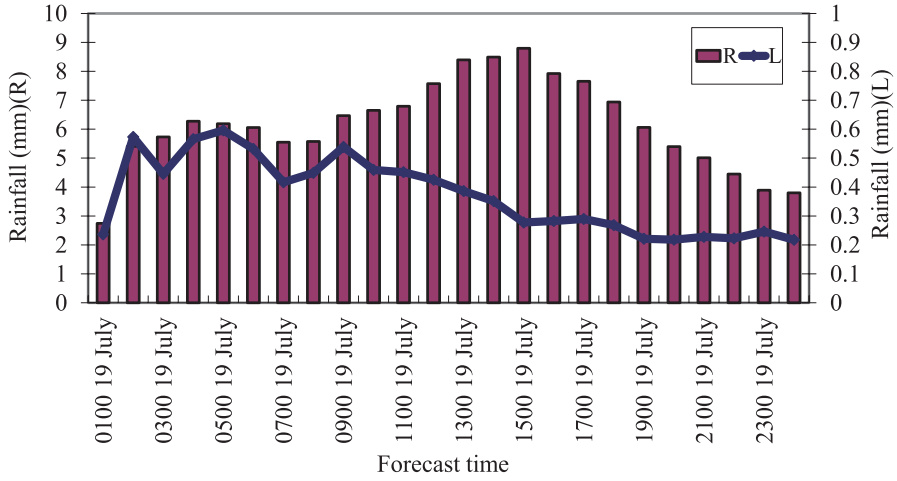

Fig. 2. Temporal evolution of the rainfall in the R (bars) and L (line) regions (units: mm).

where ξ_p is the vertical projection of the absolute vorticity, f is geostrophic vorticity, u and v are zonal and meridional wind components, respectively, p is atmospheric pressure, g is acceleration of gravity, and θ_e is potential temperature. Furthermore,

$$\mathrm{MPV}_1 = -g(\xi_p + f)\frac{\partial \theta_e}{\partial p}\,, \tag{1a}$$

$$\mathrm{MPV}_2 = g\frac{\partial v}{\partial p}\frac{\partial \theta_e}{\partial x} - g\frac{\partial u}{\partial p}\frac{\partial \theta_e}{\partial y}, \tag{1b}$$

where MPV_1 is the moist barotropic item, dependent on the vertical component of the absolute vorticity and vertical gradient of equivalent potential temperature, which represents the effects of inertial stability $(\xi_p + f)$ and convective stability $(\partial\theta_e/\partial p)$. Since absolute vorticity is always positive, when the atmosphere is convectively unstable, $\partial\theta_e/\partial p > 0$ and $\mathrm{MPV}_1 < 0$; and when the atmosphere is stable, $\partial\theta_e/\partial p < 0$ and $\mathrm{MPV}_1 > 0$. MPV_2 is the moist baroclinic item, dependent on the moist baroclinicity $(\nabla_p\theta_e)$ and vertical shear of horizontal wind. Wu et al. (1995) proposed that when the atmosphere is convectively stable $(\partial\theta_e/\partial p > 0)$ and $\mathrm{MPV}_2 > 0$, vertical vorticity increases quickly. MPV_1 (MPV_2) is less than (greater than) zero, which is deduced by slantwise-vorticity development, linked to the convective instability and baroclinic instability.

3.2. *Q vector partitioning*

The development of precipitation systems results from the interaction between multi-scale weather systems. The rainfall is related to upward motion, and its variation is associated with multi-scale upward motion. The $\boldsymbol{Q}$ vector is a powerful tool for estimating the vertical motion (Dunn, 1991). Recently, Yue (2009b) proposed an ageostrophic $\boldsymbol{Q}$ vector ($\boldsymbol{Q}_\mathrm{D}$) that can be calculated using one-layer data. In the pressure coordinate system,

$$\boldsymbol{Q}_\mathrm{D} = (Q_{\mathrm{D}x}, Q_{\mathrm{D}y}) = -\left(\frac{\partial u}{\partial x}\frac{\partial \alpha}{\partial x} + \frac{\partial v}{\partial x}\frac{\partial \alpha}{\partial y}\right)\boldsymbol{i} - \left(\frac{\partial u}{\partial y}\frac{\partial \alpha}{\partial x} + \frac{\partial v}{\partial y}\frac{\partial \alpha}{\partial y}\right)\boldsymbol{j}\,, \tag{2}$$

where $\alpha = 1/\rho = RT/p$; α is special volume, ρ is air density, R is gas constant, T is temperature, and $Q_{\mathrm{D}x}$ and $Q_{\mathrm{D}y}$ are the x and y components of $\boldsymbol{Q}_\mathrm{D}$, respectively. When geostrophic winds are used, $\boldsymbol{Q}_\mathrm{D}$ becomes the quasi-geostrophic $\boldsymbol{Q}$ vector (Hoskins et al., 1978).

The ω equation, with the forcing of $\boldsymbol{Q}_\mathrm{D}$ vector divergence, can be expressed by

$$\nabla^2(\sigma\omega) + f^2\frac{\partial^2\omega}{\partial p^2} = -2\nabla\cdot\boldsymbol{Q}_\mathrm{D}\,, \tag{3}$$

in which ω has a wave solution, and the left side of Eq. (3) is proportional to $-\omega$. Thus, $\nabla\cdot\boldsymbol{Q}_\mathrm{D} \propto \omega$. Furthermore, when $\nabla\cdot\boldsymbol{Q}_\mathrm{D} < 0, \omega < 0$; and when $\nabla\cdot\boldsymbol{Q}_\mathrm{D} > 0, \omega > 0$. The divergence of $\boldsymbol{Q}_\mathrm{D}$ can describe the vertical motion well.

Previous studies (Keyser et al., 1988, 1992; Martin, 1999, 2007; Yue et al., 2003, 2011) have shown that partitioning of the $\boldsymbol{Q}$ vector can provide useful information about the forcing from multi-scale weather systems. The $\boldsymbol{Q}$ vector is often decomposed into two components: one along the direction of potential temperature ($\boldsymbol{Q}_s$) and the other along the direction of the potential temperature gradient ($\boldsymbol{Q}_n$). $\boldsymbol{Q}_s$ represents the thermal wind direction with quasi-geostrophic characteristics, denoting large-scale information; $\boldsymbol{Q}_n$ is the geostrophic departure, denoting mesoscale weather. According to the traditional $\boldsymbol{Q}$ vector partitioning method, the $\boldsymbol{Q}_\mathrm{D}$ vector is decomposed into two parts: $\boldsymbol{Q}_{\mathrm{D}s}$ and $\boldsymbol{Q}_{\mathrm{D}n}$, and they can be expressed as follows in the p-coordinate system:

$$\boldsymbol{Q}_{\mathrm{D}n} = \left[\frac{\left(\frac{\partial\theta}{\partial x}Q_{\mathrm{D}x} + \frac{\partial\theta}{\partial y}Q_{\mathrm{D}y}\right)\frac{\partial\theta}{\partial x}}{\left(\frac{\partial\theta}{\partial x}\right)^2 + \left(\frac{\partial\theta}{\partial y}\right)^2}\right]\boldsymbol{i} + \left[\frac{\left(\frac{\partial\theta}{\partial x}Q_{\mathrm{D}x} + \frac{\partial\theta}{\partial y}Q_{\mathrm{D}y}\right)\frac{\partial\theta}{\partial y}}{\left(\frac{\partial\theta}{\partial x}\right)^2 + \left(\frac{\partial\theta}{\partial y}\right)^2}\right]\boldsymbol{j}\,, \tag{4}$$

$$\boldsymbol{Q}_{\mathrm{D}s} = \left[\frac{\left(\frac{\partial\theta}{\partial y}Q_{\mathrm{D}x} - \frac{\partial\theta}{\partial x}Q_{\mathrm{D}y}\right)\frac{\partial\theta}{\partial y}}{\left(\frac{\partial\theta}{\partial x}\right)^2 + \left(\frac{\partial\theta}{\partial y}\right)^2}\right]\boldsymbol{i} + \left[\frac{\left(-\frac{\partial\theta}{\partial y}Q_{\mathrm{D}x} + \frac{\partial\theta}{\partial x}Q_{\mathrm{D}y}\right)\frac{\partial\theta}{\partial x}}{\left(\frac{\partial\theta}{\partial x}\right)^2 + \left(\frac{\partial\theta}{\partial y}\right)^2}\right]\boldsymbol{j}\,. \tag{5}$$

Both $\boldsymbol{Q}_{\mathrm{D}s}$ and $\boldsymbol{Q}_{\mathrm{D}n}$ have the same diagnostic characteristics as $\boldsymbol{Q}_{\mathrm{D}}$, and $2\nabla\cdot\boldsymbol{Q}_{\mathrm{D}n}$ and $2\nabla\cdot\boldsymbol{Q}_{\mathrm{D}s}$ can reveal the forcing effects of different scale weather systems, the results of which are discussed later in the paper.

3.3. *Forcing of terrain*

The effects of topography on rainfall come from orographic lift and surface friction. In the pressure coordinate, vertical velocity caused by orographic lift (Zhu et al., 1992) can be written as

$$\omega_{\mathrm{T}xy} = -\rho_0 g\left(u_0\frac{\partial H_{\mathrm{h}}}{\partial x} + v_0\frac{\partial H_{\mathrm{h}}}{\partial y}\right)\,, \tag{6}$$

where H_{h} is the height of the terrain.

The vertical velocity caused by surface friction (Miller et al., 1972) is written as

$$\omega_{\mathrm{F}xy} = \frac{\rho_0 g}{f}\left[\frac{\partial}{\partial y}(C_{\mathrm{d}}u_0\sqrt{u_0^2+v_0^2}) - \frac{\partial}{\partial x}(C_{\mathrm{d}}v_0\sqrt{u_0^2+v_0^2})\right]\,, \tag{7}$$

where C_{d} is the drag coefficient ($= 2.5\times10^{-3}$). In both Eqs. (6) and (7), ρ_0 is surface air density, and u_0 and v_0 are the zonal and meridional components of surface wind, respectively.

To calculate the 3D topography-induced vertical velocity, we set $\omega = 0$ at the top boundary ($p = 100$ hPa) and $(\omega)_{\mathrm{p900}} = \omega_{\mathrm{T}xy}$ (or $\omega_{\mathrm{F}xy}$) at the low boundary. Here, the low boundary was set to 900 hPa:

$$\left.\begin{aligned}\nabla^2(\sigma\omega) + f^2\frac{\partial^2\omega}{\partial p^2} &= 0\\ (\omega)_{\mathrm{p100}} = 0, (\omega)_{\mathrm{p900}} &= \omega_{T_{xy}}\end{aligned}\right\}\,, \tag{8}$$

where vertical velocity is zero at the lateral boundaries. Stability, $\sigma = -h(\partial\theta/\partial p)[h = (R/p)(p/1000)^{R/c_p}]$ was averaged in each layer. The relaxation method was used to solve Eq. (8) and to construct the vertical velocity.

4. Results

The results of our diagnosis showed that the development of the rainfall was primarily associated with water vapor, stability and upward motion.

4.1. *Water vapor*

4.1.1. *Relative humidity*

Usually, a relative humidity (RH) of greater than 80% is a necessary condition for rainfall (Ding, 1989; Sinclair, 1994). As shown in Fig. 3a, RH was greater than 80% from 1000 hPa to 350 hPa during landfall. RH was greater than 95% from 900 hPa to 800 hPa. Over the L region (Fig. 3b), RH was greater than 80% from 900 hPa to 400 hPa. After landfall (0900 UTC 19 to 0000 UTC 20 July 2005), RH was greater than 95%. It is worth noting that RH was less than 80% below 950 hPa. RH was greater than 80% from the surface to 900 hPa over the R region, whereas it was less than 80% over the L region during the 24 h integration. The depth of RH in the R region was from 900 hPa to 400 hPa, but in the L region it was 900 hPa to 650 hPa. RH of greater than 95% appeared at 800 hPa to 900 hPa during 0300 UTC 19 July to 0000 UTC 20 July 2005 and extended to 700 hPa to 500 hPa during 1500 to 2100 UTC 19 July 2005, while the L region only featured an RH of 95% at 950 hPa to 700 hPa during 0900 UTC 19 July to 0000 UTC 20 July. The comparison reveals that the depth of RH at greater than 80% in the R region was similar to that in the L region. The main differences in the RH of 95% between the R and L regions included the following: (1) the R region led the L region by 6 h and the R region lasted longer than the L region; and (2) the depth was greater in the R region than in the L region; and (3) during 1500 to 2100 UTC 19 July 2005, the R region extended to 700 hPa to 500 hPa. Thus, the RH in both the R and L regions was greater than 80% and the R region held more water vapor than the L region.

4.1.2. *Water flux and its divergence*

The transport of water vapor is an important source for rainfall development. The water vapor flux ($q\boldsymbol{V}/g$) and its divergence $[(1/g)\nabla\cdot(\boldsymbol{V}q)]$ can depict the water vapor transport. Before 1200 UTC 19 July 2005, easterly and southeasterly winds transported water vapor to the R region, while northerly and northwesterly winds transported water vapor to the L region (Fig. 4). The convergence of water vapor flux ($> 0.1\times10^{-6}$ g cm^{-2} hPa^{-1} s^{-1}) in the R region appeared in the range 1000–800 hPa, and the other convergence zone occurred in the range 600–300 hPa at 0900–1500 UTC 19 July 2005. In the L region, the convergence of water vapor flux (0.1×10^{-6} g cm^{-2} hPa^{-1} s^{-1}) appeared in the range 1000–800 hPa, and the convergence of water vapor flux occurred in the range 800–300 hPa at 0100–1500 UTC 19 July 2005. The convergence of water vapor flux was 10 times larger in the R region than in the L region.

Typhoon Haitang (2005) made landfall in Fujian Province, China. The mountains in this region are oriented in the northeast–southwest direction (Fig. 1a). The easterly and southeasterly winds (Fig. 4a) on the right side of the typhoon

track transported water vapor from the ocean to the rainfall region. On the left side of the track (Fig. 4b), westerly winds on the leeward slope transported dry air to the typhoon center. This caused asymmetric rainfall and is further analyzed in section 4.3.2.

4.2. *Stability*

Bennetts and Hoskins (1979) proposed conditional symmetric instability (CSI), which is moist hydrostatic inertial instability. CSI represents one of the mechanisms that explain the development of slantwise convection, which has a close relationship with severe storms. The atmosphere usually possesses convective stability and inertial stability, but CSI is very likely to occur when upward slantwise motion takes place. MPV represents dynamic, thermodynamic and water vapor effects. Bennetts and Hoskins (1979) showed that when MPV is negative (MPV < 0), CSI may occur. MPV theory has been applied widely in analyses of the precipitation of landfalling typhoons for several decades (Wang and Chen, 1997; Zhao and Wu, 2004; Lai et al., 2007; Huang et al., 2009).

4.2.1. *Spatiotemporal comparison of* MPV

Figures 5a and b show the appearance in the R region of negative MPV in the range 900–1000 hPa, with a maximum

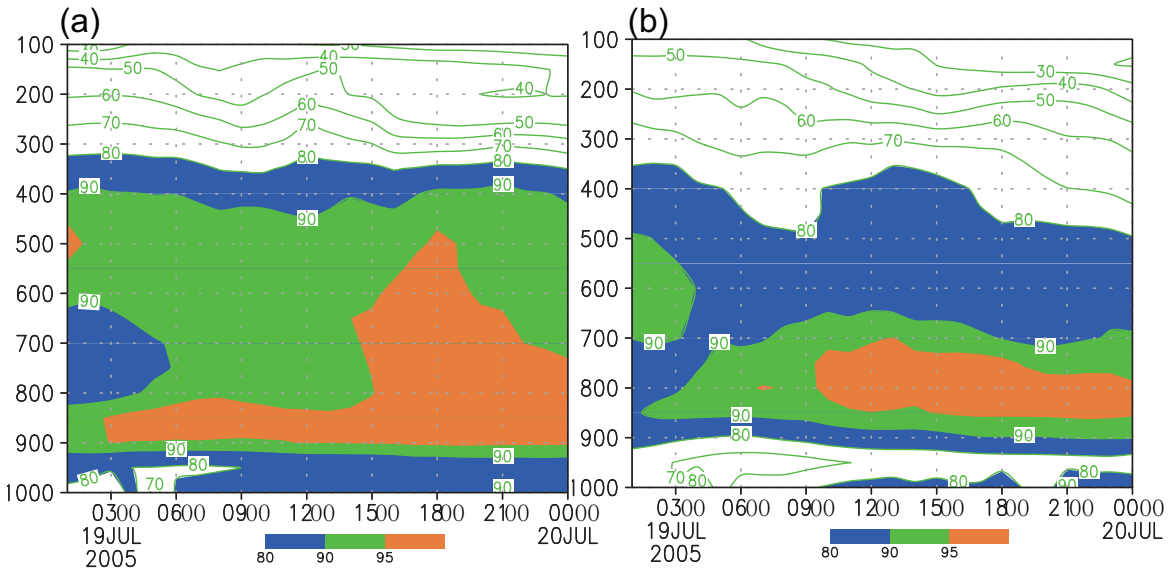

Fig. 3. Temporal evolution of RH (units: %) in the (a) R and (b) L regions.

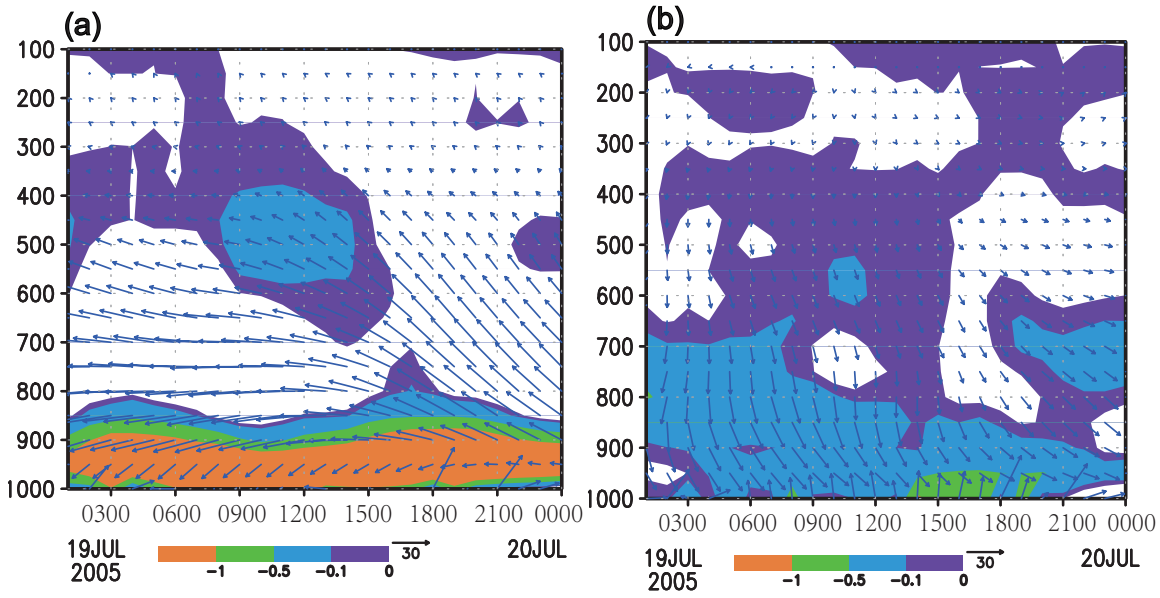

Fig. 4. Temporal evolution of water vapor flux (units: g cm^{-1} hPa^{-1} s^{-1}) and its divergence (units: 10^{-6} g cm^{-2} hPa^{-1} s^{-1}) in the (a) R and (b) L regions.

of −2.0 PVU (1 PVU=10^{-6} K m^2 kg^{-1} s^{-1}). During 1800 UTC 19 July to 0000 UTC 20 July 2005, negative MPV also occurred in the range 900–700 hPa. In the L region, negative MPV mainly occurred in the range 900–1000 hPa, with a maximum of −3.5 PVU; and during 0100–0900 UTC 19 July 2005, negative MPV appeared in the range 900–800 hPa. The comparison suggests that negative MPV mainly appeared in the range 900–1000 hPa and the MPV in the L region was stronger than that in the R region.

4.2.2. *Comparison of* MPV1

Figures 5c and d show that, in the R region, negative MPV_1 occurred in the range 800–1000 hPa, with a maximum of −2.0 PVU. Negative MPV_1 also appeared in the range 800–700 hPa during 1800 UTC 19 July to 0000 UTC 20 July 2005. In the L region, negative MPV_1 mainly appeared in the range 900–1000 hPa, with a maximum of −3.5 PVU, meanwhile, negative MPV_1 occurred in the range 900–800 hPa during 0100–0900 UTC 19 July 2005. The comparison reveals that negative MPV_1 mainly appeared in the range 900–1000 hPa and that the MPV_1 in the L region was stronger than that in the R region. Further analysis showed that the distribution of negative MPV_1 was similar to positive $\partial\theta_e/\partial p$. Thus, there was convective instability in the lower troposphere in both the R and L regions, but it was stronger in the L region.

4.2.3. *Comparison of* MPV_2

Figures 5e and f show that, in the range 900–1000 hPa, MPV_2 was generally positive in the R region, with a maximum of 1 PVU, and negative above 800 hPa. In the L region, positive MPV_2 occurred in the range 900–1000 hPa, and negative MPV_2 appeared above 900 hPa. The former MPV_2 was stronger than the latter in the range 1000–800 hPa.

Comparison between MPV_2 and MPV_1 indicates that, in the R region, the MPV_1 and MPV_2 were out of phase, and that the $MPV_1 > 0$ ($MPV_1 < 0$) responded to $MPV_2 < 0$ ($MPV_2 > 0$). The criteria of $MPV_1 < 0$ and $MPV_2 > 0$ was outstanding in the R region. Thus, the R region was more conducive to the development of rainfall than the L region.

4.3. *Vertical motion*

Rainfall associated with upward motion is the secondary circulation. Figure 6a shows that, before landfall, upward motion in the lower troposphere was stronger than in the upper troposphere. The maximum upward motion of −1.3 Pa s^{-1} appeared at 850 hPa. During landfall, the upward motion weakened in the range 900–600 hPa and its maximum was −0.8 Pa s^{-1} at 850 hPa. Upward motion enhanced in the range 400–200 hPa and its maximum reached −0.5 Pa s^{-1}. This may have been related to the coastal terrain. After landfall, upward motion increased to −0.5 Pa s^{-1}. Upward motion of −1.0 Pa s^{-1} occurred in the ranges 450–200 hPa and 900–700 hPa. From 1500–1800 UTC 19 July 2005, upward motion increased continuously in the range 900–500 hPa, but decreased above 500 hPa. During 1800 UTC 19 July to 0000 UTC 20 July 2005, upward motion weakened below 500 hPa. This suggests that there was always upward motion in the R region. During landfall, upward motion became weak. Twelve hours after landfall, upward motion increased again. Figure 6b shows that upward motion mainly appeared below 700 hPa and its maximum was −0.3 Pa s^{-1}. During landfall, upward motion decreased gradually and, after landfall, it barely changed. It is worth noting that the maxima of upward motion in the R region were about five times stronger than those in the L region, which was conducive to the asymmetric distribution of rainfall. Next, we analyzed the contributions of different scale weather systems and terrain to upward motion.

4.3.1. *Forcing of different-scale weather systems*

Before landfall, the convergence of the $\boldsymbol{Q}_{Ds}$ vector occurred in the ranges 1000–900 hPa and 400–200 hPa, with a maximum of -0.03×10^{-13} hPa^{-1} s^{-3} (Fig. 7a). After landfall, it weakened in the lower troposphere. During 0900–1600 UTC 19 July 2005, the convergence of $\boldsymbol{Q}_{Ds}$ was enhanced in the range 700–200 hPa and its maximum was -0.03×10^{-13} hPa^{-1} s^{-3} at 550 hPa. During 1500–2000 UTC 19 July 2005, the convergence of $\boldsymbol{Q}_{Ds}$ appeared in the range 850–500 hPa and the maximum was -0.03×10^{-13} hPa^{-1} s^{-3} at 700 hPa. The convergence of $\boldsymbol{Q}_{Ds}$ moved downward. The low-level convergence of the $\boldsymbol{Q}_{Ds}$ vector weakened after landfall but it was enhanced in the upper troposphere. The convergence of the $\boldsymbol{Q}_{Ds}$ vector mainly appeared in the ranges 800–900 hPa and 600–450 hPa (Fig. 7b). The convergence depth in the air column and the intensity of the $\boldsymbol{Q}_{Ds}$ vector almost barely changed. Comparing Figs. 7a and b shows that the convergence intensity of the former was much stronger than the latter, indicating that the large-scale forcing in the R region was stronger, and there was a greater contribution to the difference in rainfall intensity, compared to in the L region.

The convergence of $\boldsymbol{Q}_{Dn}$ mainly occurred in the range 1000–800 hPa during landfall and, after landfall, it weakened (Fig. 7c). Before landfall, the convergence of $\boldsymbol{Q}_{Dn}$ mainly appeared in the range 500–200 hPa, with a maximum of -0.08×10^{-13} hPa^{-1} s^{-3} at 350 hPa. After landfall, the convergence of the $\boldsymbol{Q}_{Dn}$ vector of -0.06×10^{-13} hPa^{-1} s^{-3} moved downward to 500–350 hPa, but was enhanced to -0.12×10^{-13} hPa^{-1} s^{-3} at 400 hPa. During 1700–2100 UTC 19 July 2005, the maximum of -0.06×10^{-13} hPa^{-1} s^{-3} appeared in the range 700–500 hPa, and it was maintained but moved downward persistently. From the above analysis, the convergence of $\boldsymbol{Q}_{Dn}$ in the lower troposphere decreased and the convergence in the lower troposphere increased after landfall. The convergence of $\boldsymbol{Q}_{Dn}$ moved downward. During landfall, the convergence of $\boldsymbol{Q}_{Dn}$ barely changed (Fig. 7d). The comparison between the R and L regions reveals that the convergence of $\boldsymbol{Q}_{Dn}$ was more intensive and thicker in the R region than in the L region. Thus, the R region possessed stronger mesoscale forcing than the L region, which contributed to the asymmetric rainfall distribution.

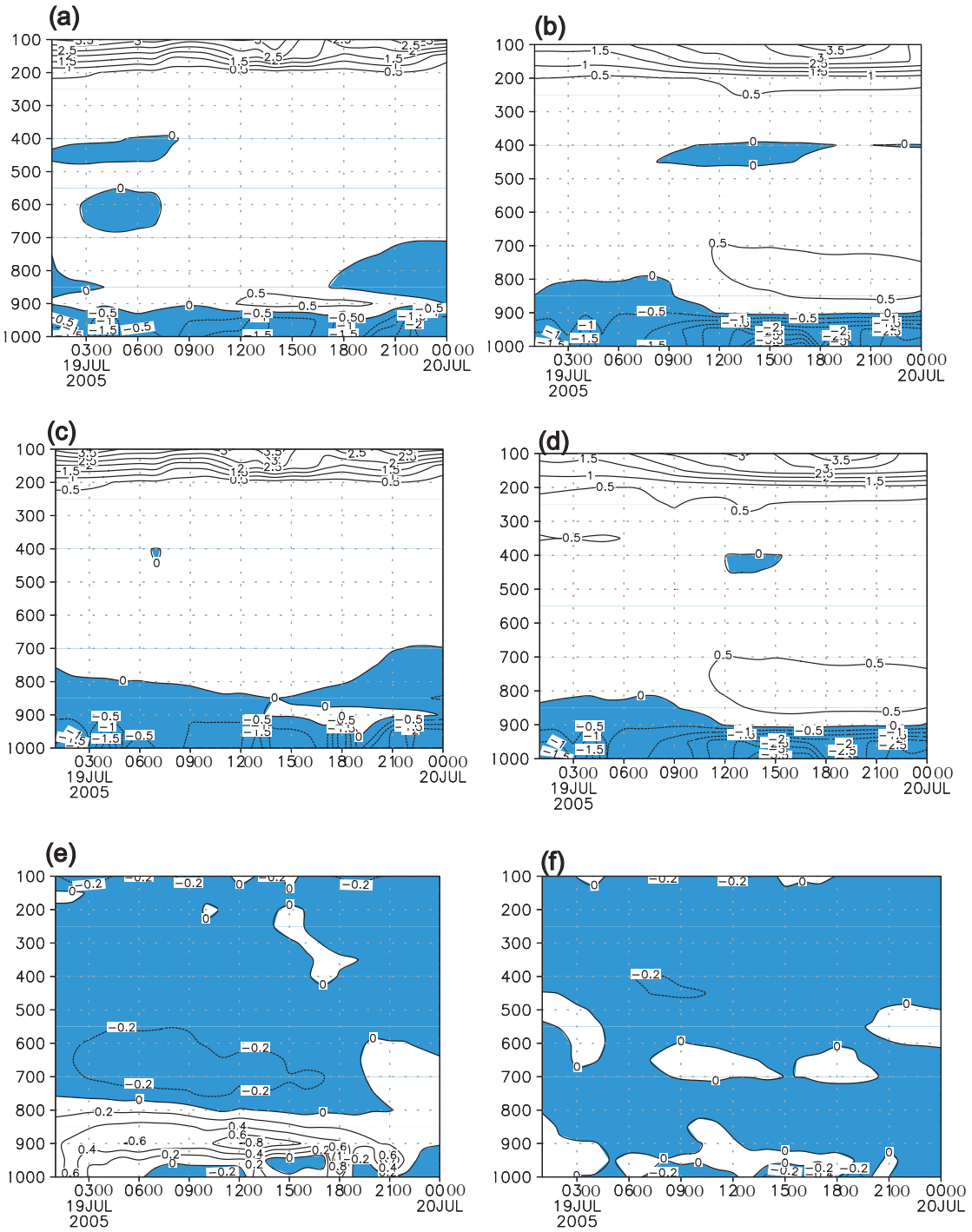

Fig. 5. Temporal evolution of MPV in the (a) R and (b) L regions, MPV_1 in the (c) R and (d) L regions, and MPV_2 in the (e) R and (f) L regions (solid line = positive; dashed line = negative; units: PVU, 1 PVU = 10^{-6} K m^2 s^{-1} kg^{-1}).

4.3.2. *Forcing of terrain*

Figure 8a shows that, during landfall, orographic lift forced upward motion, and that upward motion decreased rapidly with height. Upward motion at 800 hPa was only about one ninth of that near the surface. Downward motion occurred (Fig. 8b). The difference in vertical velocity between the R and L regions caused the asymmetric rainfall distribution.

Surface friction produced downward motion before landfall and generated upward motion after landfall (Fig. 8c). Upward motion decreased rapidly. Upward motion at 700 hPa was about one order of magnitude smaller than that near the surface. Surface friction forced upward motion during landfall, and it decreased rapidly with height (Fig. 8d). Upward motion at 700 hPa was about one seventh of that near the surface. The comparison shows that, before landfall, downward motion appeared in the R region but upward motion occurred in the L region. After landfall, friction-induced upward mo-

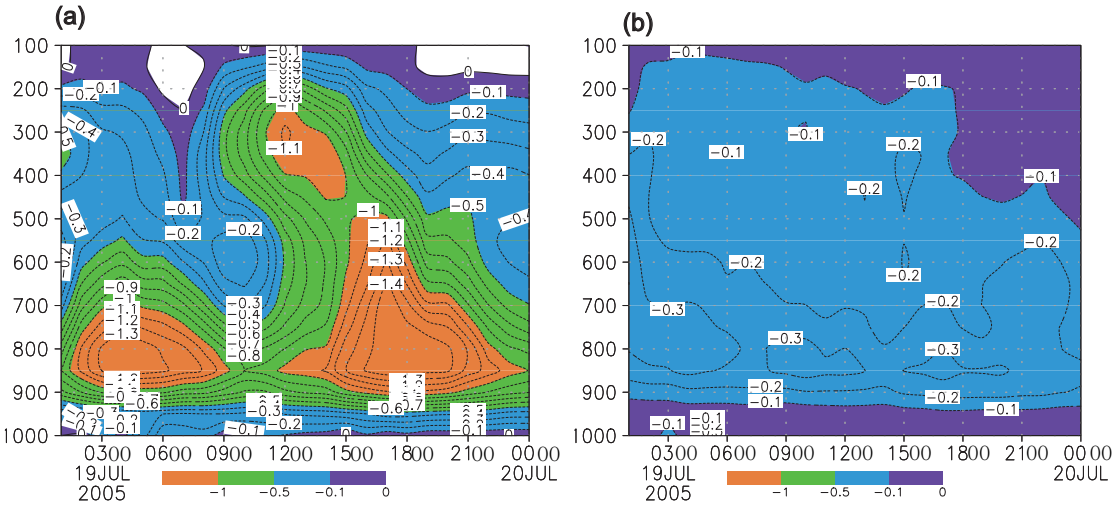

Fig. 6. Temporal evolution of vertical motion in the (a) R and (b) L regions (solid line = downward motion; dashed line = upward motion; units: Pa s^{-1}).

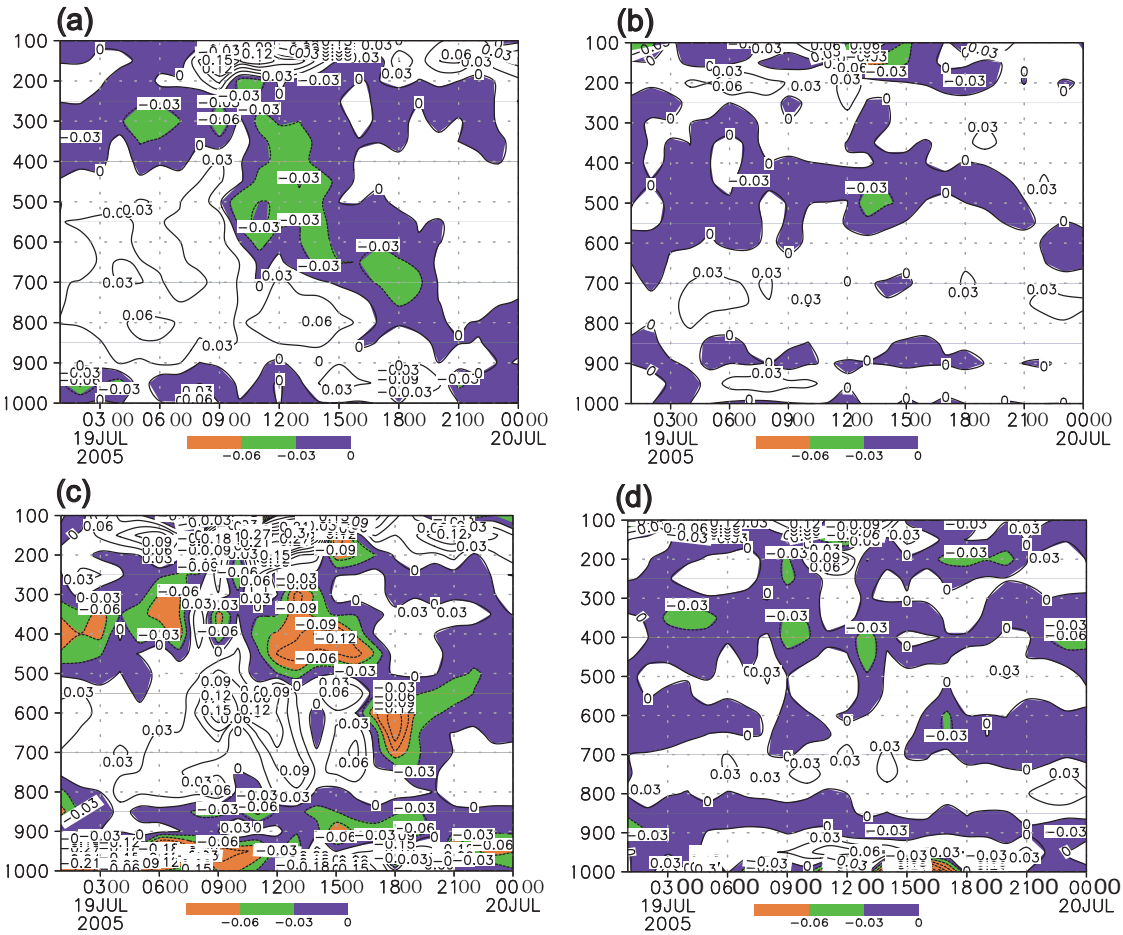

Fig. 7. Temporal evolution of (a, b) $\boldsymbol{Q}_{\mathrm{D}s}$ and (c, d) $\boldsymbol{Q}_{\mathrm{D}n}$ in the (a, c) R and (b, d) L regions (solid line = divergence; dashed line = convergence; units: 10^{-13} hPa^{-1} s^{-3}).

tion was present in both the R and L regions. The magnitude of upward motion was twice as large in the R region than in the L region, which was conducive to the development of the asymmetric rainfall distribution.

5. Summary

The 24-hour accumulated precipitation data for typhoon Haitang (2005) reveal an asymmetric rainfall distribution be-

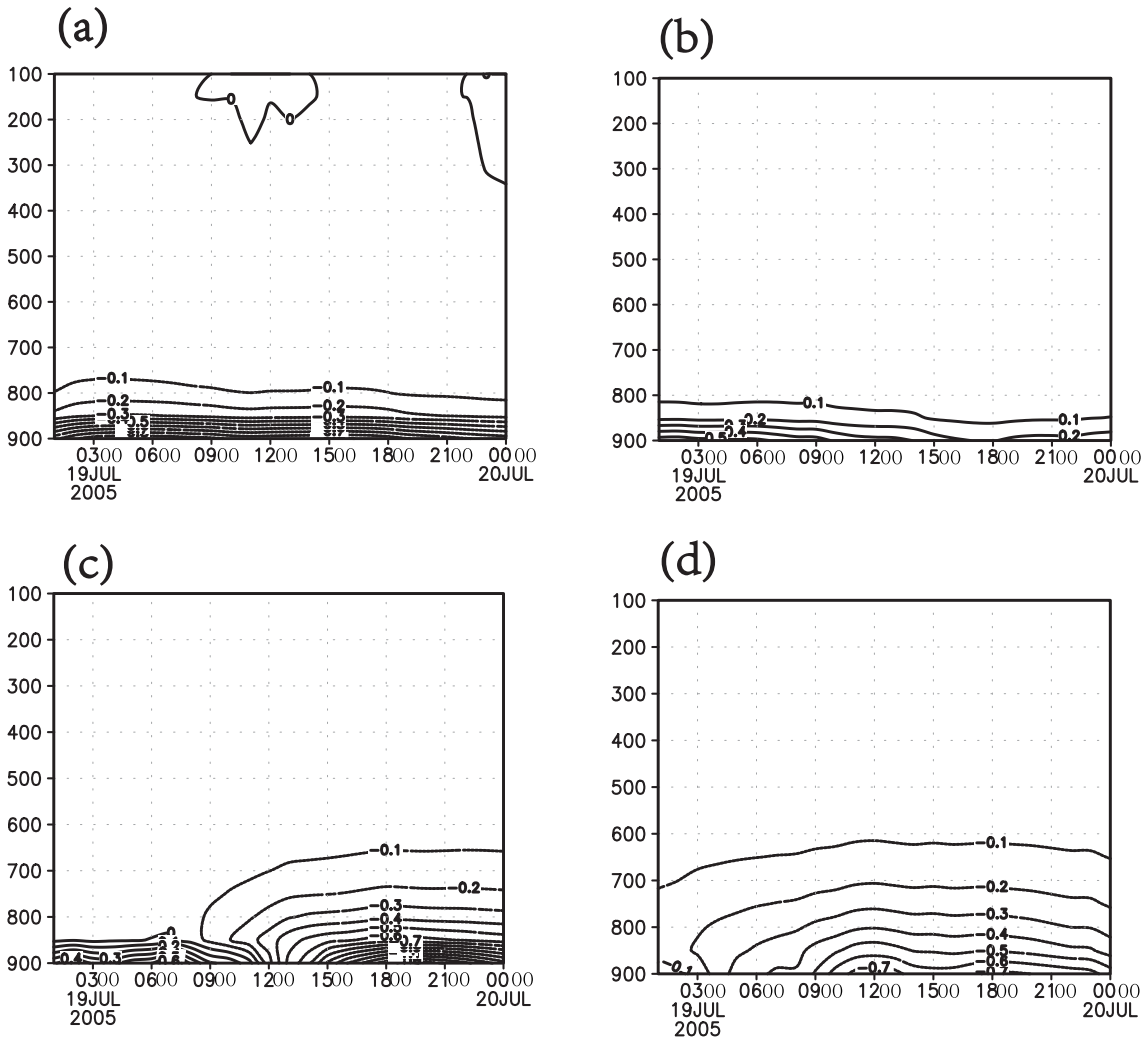

Fig. 8. Temporal evolution of vertical motion forced by (a, b) orographic lift and (c, d) surface friction in the (a, c) R and (b, d) L regions (solid line = downward motion; dashed line = upward motion; units: Pa s^{-1}).

tween each side of its track. The WRF model successfully simulated this asymmetric distribution. Analysis of the simulated hourly high-resolution data showed that the rain rate was about 15 times larger on the right side of the track than on the left side. The major results from the diagnostic study were as follows:

(1) The calculations of RH, water vapor flux and its divergence indicated that there was sufficient water vapor with RH greater than 80% on both sides, but the right side was more humid than the left side. Easterly and southeasterly winds transported water vapor to the right side, while northerly wind transported water vapor to the left side. The convergence of water vapor flux on the right side was stronger than on the left side.

(2) The MPV results revealed that both sides featured CSI (MPV$<$0). Slantwise vorticity development ($MVP_1 < 0$ and $MPV_2 > 0$) was more favorable on the right side than on the left side.

(3) Upward motion was significantly different between the right and left sides. The right side had stronger upward motion than the left side. Analysis of the $\boldsymbol{Q}$ vector demonstrated that both large-scale and mesoscale forcing were attributable to the rainfall difference between the two sides. The forcing of orographic lift produced upward and downward motion over the right and left sides, respectively. Surface friction contributed to the asymmetric rainfall structures after landfall.

On the right side, there was stronger water vapor flux and unstable energy, followed by stronger upward motion that released a substantial amount of unstable energy and that transported the water vapor from the lower troposphere to the upper troposphere, which in turn promoted the development of rainfall. On the left side, weak baroclinic instability was associated with weak water vapor flux, and weak upward motion in the lower troposphere only triggered the weak release of unstable energy and upward transport of water vapor, which in turn weakened the development of rainfall. This led to the asymmetric distribution of rainfall between the two sides of the track.

The asymmetric rainfall distribution in this study was pri-

marily associated with humidity, stability and vertical upward motion forced by multi-scale systems. Terrain also played an important role in the production of the distribution. In more general terms, many other factors, and the differences among them, can affect and result in an asymmetric distribution of rainfall. In this study, only macroscopical factors, such as water vapor, stability and vertical motion, have been discussed. However, microphysical processes are also important, which we intend to examine in future work.

Acknowledgements. This work was supported by Public Sector (Meteorology) Research of China (Grant Nos. GYHY 201306012 and GYHY201506007), the National Natural Science Foundation of China (Grant Nos. 40875025, 41175050, 41475039 and 41475041), and the Shanghai Natural Science Foundation of China (Grant No. 08ZR1422900).

REFERENCES

Bender, M. A., R. E. Tuleya, and Y. A. Kurihara, 1985: A numerical study of the effect of a mountain range on a landfalling tropical cyclone. *Mon. Wea. Rev*., **113**, 567–582.

Bennetts, D. A., and B. J. Hoskins, 1979: Conditional symmetric instability—a possible explanation for frontal rainbands. *Quart. J. Roy. Meteor. Soc.*, **105**, 945–962.

Chan, J. C., and X. D. Liang, 2003: Convective asymmetries associated with tropical cyclone landfall. Part I: f-plane simulations. *J. Atmos. Sci.*, **60**, 1560–1567.

Chen, L. S., X. D. Xu, Z. X. Luo, and J. Z. Wang, 2002: *Introduction to Dynamics of Tropical Cyclone*. China Meteorological Press, Beijing, 211–313. (in Chinese)

Chen, L. S., and Y. H. Ding, 1979: *Outline of the Western Pacific Typhoon*. Science Press, Beijing, 440–488 pp. (in Chinese)

Chen, L. S., and Z. Y. Meng, 2001: An overview on tropical cyclone research progress in China during the past ten years. *Chinese J. Atmos. Sci*., **25**, 420–432. (in Chinese)

Chen, L. S., Z. X. Luo, and Y. Li, 2004: Research advances on tropical cyclone landfall process. *Acta Meteorologica Sinica*, **62**, 541–549. (in Chinese)

Cline, I. M., 1926: *Tropical cyclones*. MacMillan Co., New York, N. Y., 301 pp.

Ding, Y. H., 1989: *Diagnostic and Analytical Methods in Synoptic Dynamics*. Science Press, Beijing, 114–116. (in Chinese)

Ding, Z. Y., Y. Wang, X. Y. Shen, and H. M. Xu, 2009: On the causes of rainband breaking and asymmetric precipitation in typhoon Haitang (2005) before and after its landfall. *J. Trop. Meteor*., **25**, 513–520. (in Chinese)

Dunn, G. E., and B. I. Miller, 1964: *Atlantic Hurricanes.* Louisiana State University Press, 377 pp.

Dunn, L. B., 1991: Evaluation of vertical motion: Past, present, and future. *Wea. Forecasting*, **6**, 65–73.

Dudhia, J., 1989: Numerical study of convection observed during the Winter Monsoon Experiment using a mesoscale two-dimensional model. *J. Armos. Sci*., **46**, 3077–3107.

Ek, M. B., K. E. Mitchell, Y. Lin, E. Rogers, P. Grunmann, V. Koren, G. Gayno, and J. D. Tarpley, 2003: Implementation of Noah land surface model advances in the National Centers for Environmental Prediction operational mesoscale Eta Model. *J. Geophys*. Res., **108**, 8851, doi: 10.1029/2002JD003296.

Frank, W. M., 1977: The structure and energetics of the tropical cyclone. Part I: Storm structure. *Mon. Wea. Rev*., **105**, 1119–1135.

Hong, S.-Y., and H.-L. Pan, 1996: Nonlocal boundary layer vertical diffusion in a medium-range forecast model. *Mon. Wea. Rev*., **124**, 2322–2339.

Hoskins, B. J., I. Draghici, and H. C. Davies, 1978: A new look at the ω-equation. *Quart. J. Roy. Meteor. Soc*., **104**, 31–38.

Huang, Y., S. W. Shou, and L. Y. Fu, 2009: A diagnostic analysis of PV and MPV on the heavy rain caused by typhoon Khanun. *Meteorological Monthly*, **35**, 65–73. (in Chinese)

Ji, C. X., G. Y. Xue, F. Zhao, Z. S. Yu, and H. Zhang, 2007: The numerical simulation of orographic effect on the rain and structure of typhoon Rananim during landfall. *Chinese J. Atmos. Sci*., **31**, 233–244. (in Chinese)

Jones, R. W., 1987: A simulation of hurricane landfall with a numerical model featuring latent heating by the resolvable scales. *Mon. Wea. Rev*., **115**, 2279–2297.

Kain, J. S., and J. M. Frisch, 1993: *Convective Parameterization for Mesoscale Models: The Kain-Fritsch Scheme.* The Representation of Cumulus Convection in Numerical Models, Meteor. Monogr., No. 46, Amer. Meteor. Soc., 165–170.

Keyser, D., M. J. Reeder, and R. J. Reed, 1988: A generalization of Petterssen's frontogenesis function and its relation to the forcing of vertical motion. *Mon. Wea. Rev*., **116**, 762–781.

Keyser, D., B. D. Schmidt, and D. G. Duffy, 1992: Quasi-geostrophic vertical motions diagnosed from along-and cross-isentrope components of the $\boldsymbol{Q}$ vector. *Mon. Wea. Rev*., **120**, 731–741.

Lai, S. J., F. He, R. T. Zhao, T. L. Shen, and Q. S. Wu, 2007: The diagnostic analysis of "Longwang" typhoon. *Scientia Meteorologica Sinica*, **27**, 266–271. (in Chinese)

Li, S. Y., Z. Y. Ding, and N. Zhou, 2007: Numerical simulation and diagnostic analysis of the southern rainstorm of 0307 typhoon "Imbudo" influencing Guangxi. *Journal of Oceanography in Taiwan Strait*, **26**, 204–212. (in Chinese)

Lin, Y. L., D. B. Enskey, and S. Chiao, 2002: Orographic influences on rainfall and track deflection associated with the passage of a tropical cyclone. *Mon. Wea. Rev.*, **130**, 2929–2950.

Lin, Y.-L., R. D. Farley, and H. D. Orville, 1983: Bulk parameterization of the snow field in a cloud model. *J. Appl. Meteor*., **22**, 1065–1092.

Malwer, E. J., S. J. Taubman, P. D. Brown, M. J. Iacono, and S. A. Clough, 1997: Radiative transfer for inhomogeneous atmospheres: RRTM, a validated correlated correlated-k model for the long-wave. *J. Geophys. Res*., **102D**, 16663–16682.

Marks, F. D. Jr., 1985: Evolution of the structure of precipitation in Hurricane Allen (1980). *Mon. Wea. Rev*., **113**, 909–930.

Martin, J. E., 1999: Quasi-geostrophic forcing of ascent in the occluded sector of cyclones and the trowel airstream. *Mon. Wea. Rev*., **127**, 70–88.

Martin, J. E., 2007: Lower-tropospheric height tendencies associated with the shearwise and transverse components of quasi-geostrophic vertical motion. *Mon. Wea. Rev*., **135**, 2803–2809.

Miller, B. I., 1958: Rainfall rates in Florida hurricanes. *Mon. Wea. Rev*., **86**, 258–264.

Miller, B. I., P. P. Chase, and B. R. Jarvinen, 1972: Numerical prediction of tropical weather systems. *Mon. Wea. Rev*., **100**, 825–835.

Niu, X. X., H. L. Du, and J. Y. Liu, 2005: The numerical simulation of rainfall and precipitation mechanism associated with typhoons Sinlaku (0216). *Acta Meteorologica Sinica*, **63**, 57–

68. (in Chinese)

Parrish, J. R., R. W. Burpee, F. D. Marks Jr., and R. Grebe, 1982: Rainfall patterns observed by digitized radar during the landfall of hurricane Frederic (1979). *Mon. Wea. Rev*., **110**, 1933–1944.

Powell, M. D., 1982: The transition of the Hurricane Frederic boundary-layer wind field from the open Gulf of Mexico to landfall. *Mon. Wea. Rev*., **110**, 1912–1932.

Powell, M. D., 1987: Changes in the low-level kinematic and thermodynamic structure of Hurricane Alicia (1983) at landfall. *Mon. Wea. Rev*., **115**, 75–99.

Si, G. W., 1990: *Torrential Rain and Severe Convective System*. China Meteorological Press, Beijing, 128 pp. (in Chinese)

Sinclair, M. R., 1994: A diagnostic model for estimating orographic precipitation. *J. Appl. Meteor*., **33**, 1163–1175.

Tao, S. Y., 1980: *Torrential Rain of China*. Science Press, Beijing, 132 pp. (in Chinese)

Tao, Z. Y., B. J. Tian, and W. Huang, 1994: Asymmetry structure and torrential rain of landing typhoon 9216. *Journal of Tropical Meteorology*, **10**, 69–77. (in Chinese)

Tuleya, R. E., and Y. Kurihara, 1978: A numerical simulation of the landfall of tropical cyclones. *J. Atmos. Sci*., **35**, 242–257.

Wang, C.-C., H.-C. Kuo, Y.-H. Chen, H.-L. Huang, C.-H. Chung, and K. Tsuboki, 2012: Effects of asymmetric latent heating on typhoon movement crossing Taiwan: The case of Morakot (2009) with extreme rainfall. *J. Atmos. Sci*., **69**, 3172–3196.

Wang, J., Z. J. Ke, and J. X. Jiang, 2007: A diagnostic analysis to the asymmetric distribution of typhoon rainfall area. *J. Trop. Meteor*., **23**, 563–568. (in Chinese)

Wang, Y., Z. Y. Ding, X. Li, and Q. Wang, 2010: Dynamic analysis of asymmetric spiral rain bands around the landing of typhoon Haitang (2005). *J. Trop. Meteor*., **16**, 143–153. (in Chinese)

Wang, S. J., and G. F. Chen, 1997: A study on the criterion for interpreting typhoon heavy rain location. *J. Appl. Meteor*., **8**, 167–174. (in Chinese)

Wu, G. X., Y. P. Cai, and X. J. Tang, 1995: Moist potential vorticity and slantwise vorticity development. *Acta Meteorologica Sinica*, **53**, 387–405. (in Chinese)

Wu, L. G., J. Liang, and C.-C. Wu, 2011: Monsoonal influence on Typhoon Morakot (2009). Part I: Observational analysis. *J. Atmos. Sci*., **68**, 2208–2221.

Yang, M.-J., S. A. Braun, and D.-S. Chen, 2011: Water budget of typhoon Nari (2001). *Mon. Wea. Rev*., **139**, 3809–3828.

Yue, C. J., 2009a: A quantitative study of asymmetric characteristic genesis of precipitation associated with typhoon Haitang. *Chinese J. Atmos. Sci*., **33**, 51–70. (in Chinese)

Yue, C. J., 2009b: The $\boldsymbol{Q}$ vector analysis of the heavy rainfall from Meiyu Front cyclone: A case study. *Acta Meteorologica Sinica*, **23**, 68–80.

Yue, C.-J., and Y. Cao, 2014: Study on the genesis of asymmetrical distribution characteristics of precipitation associated with the typhoon Haitang (2005) from the viewpoint of atmospheric factor. *J. Trop. Meteor*., **30**, 219–228. (in Chinese)

Yue, C. J., S. W. Shou, K. P. Lin, and X. P. Yao, 2003: Diagnosis of the heavy rain near a Meiyu front using the wet $\boldsymbol{Q}$ vector partitioning method. *Adv. Atmos. Sci*., **20**, 37–44, doi: 10.1007/BF03342048.

Yue, C.-J., S.-W. Shou, G. Zeng, and Y.-Q. Wang, 2008: Preliminary study on asymmetric cause of formation of precipitation associated with typhoon Haitang. *Plateau Meteorology*, **27**, 1334–1342. (in Chinese)

Yue, C.-J., X.-Q. Lu, X. F. Li, and Z.-P. Zong, 2011: A study of partitioning $\boldsymbol{Q}$ vector on background conditions of a torrential rainfall over Shanghai, China on 25 August 2008. *J. Trop. Meteor*., **17**, 231–247.

Zhao, Y., and Z.-M. Wu, 2004: An analysis of the potential vorticity for the northward typhoon 9711 evolution and rainstorm. *Journal of Ocean University of China*, **34**, 13–21. (in Chinese)

Zhu, Q. G., J. R. Lin, S. W. Shou, and D. S. Tang, 1992: *Synoptic Principle and Method*. China Meteorological Press, Beijing, 322–464. (in Chinese)